The reader is about to embark on a tutorial journey through a series of nonlinear dynamic systems that contain a rich tapestry of phenomena and solutions. The study of nonlinear systems can be greatly enhanced by the combined use of the stochastic dynamic equations and Monte Carlo calculations. When a dynamic system is forced and dissipative all the trajectories tend toward a bounded set of zero volume - often a strange attractor with a fractal dimension. The stochastic dynamic equations can directly reveal the statistical moments of the system, but their direct solution is inefficient, and they are not a closed set. The power of the combined method is that the time averaged Monte Carlo moments will agree exactly with equations described by the left hand side of the full stochastic dynamic equations set to zero - no closure is required. Every equation expresses an exact relationship among the variables. One is able to delve far deeper into the nature of the nonlinear systems. This tutorial exposition offers the tools for the past nonlinear modeling efforts in the traditional physical sciences and in various complex modeling problems in new fields of biology and health sciences.

Dr. Rex J. Fleming is a mathematician with a Ph.D.in Atmospheric Science from the University of Michigan. He has over 50 years experience in government and industry as a scientist and manager in weather and climate research. He is a Dept. of Commerce Gold Medal winner and an Elected Fellow in the American Association for the Advancement of Science.

978-3-659-71514-3

Application to explosive instability

Fleming

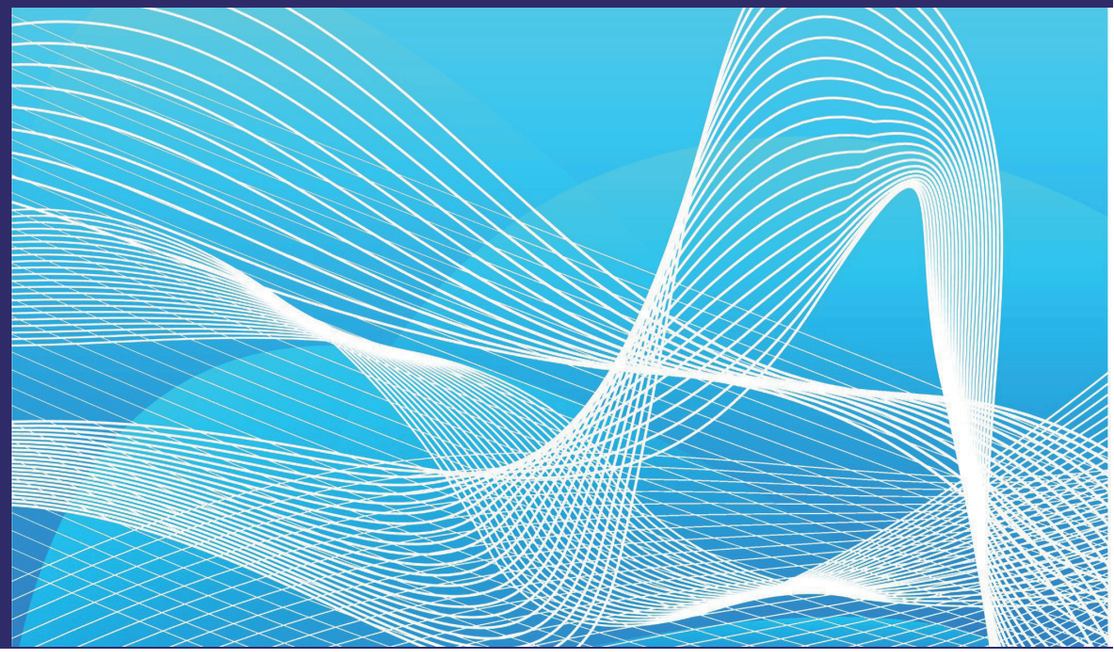

Rex J. Fleming

Analysis of the SDE/Monte Carlo Approach in Studying Nonlinear Systems

and its use in understanding the atmosphere's strange attractor associated with explosive baroclinic instability

LAP LAMBERT Academic Publishing

Rex J. Fleming

Analysis of the SDE/Monte Carlo Approach in Studying Nonlinear Systems

Rex J. Fleming

Analysis of the SDE/Monte Carlo Approach in Studying Nonlinear Systems

and its use in understanding the atmosphere's strange attractor associated with explosive baroclinic instability

LAP LAMBERT Academic Publishing

Impressum / Imprint
Bibliografische Information der Deutschen Nationalbibliothek: Die Deutsche Nationalbibliothek verzeichnet diese Publikation in der Deutschen Nationalbibliografie; detaillierte bibliografische Daten sind im Internet über http://dnb.d-nb.de abrufbar.

Bibliographic information published by the Deutsche Nationalbibliothek: The Deutsche Nationalbibliothek lists this publication in the Deutsche Nationalbibliografie; detailed bibliographic data are available in the Internet at http://dnb.d-nb.de.

Coverbild / Cover image: www.ingimage.com

Verlag / Publisher:
LAP LAMBERT Academic Publishing
ist ein Imprint der / is a trademark of
OmniScriptum GmbH & Co. KG
Heinrich-Böcking-Str. 6-8, 66121 Saarbrücken, Deutschland / Germany
Email: info@lap-publishing.com

Herstellung: siehe letzte Seite /
Printed at: see last page
ISBN: 978-3-659-71514-3

Table of Contents

Chapter 1

Introduction

The reader is about to embark on a journey through a series on nonlinear dynamic systems that contain a rich tapestry of phenomena and solutions. Perhaps observations of the attractors encountered will be enhanced by the rather new analysis procedure presented. There will be a few surprises along the route and a couple of new attractors.

The study of nonlinear systems can be embellished by the combined use of stochastic dynamic equations and Monte Carlo (MC) calculations – referred to here as the combined SDE/MC approach. The integrated use of these two mathematical tools will be demonstrated on four different nonlinear systems which exhibit chaos and strange attractors. The illumination of the attributes of the combined system is one purpose of this study. The second purpose is to use the SDE/MC approach to delve deeper into the nature of the powerful atmospheric strange attractor associated with explosive baroclinic instability.

While the age of the Earth is estimated to be 4.6 billion years old, the atmosphere has been in perpetual motion only for the last 4.0 billion years since it was formed. The solar heating of our rotating planet drives the atmospheric motion and frictional dissipation, primarily from surface friction of the winds streaming over the land and driving the ocean currents, forms a forced dissipative system. The primary mechanism driving the atmospheric circulation is baroclinic instability – other drivers are briefly mentioned later.

Differential heating between the incoming solar radiation and the outgoing infrared radiation creates a pole-to equator temperature gradient and produces a growing supply of zonal mean available potential energy. Eventually, the zonal thermal wind, developing to geostrophically balance that temperature gradient, becomes baroclinically unstable. The resulting baroclinic waves transport warm air and moisture poleward and cold air toward the equator. At the same time, the eddy available potential energy is converted to eddy kinetic energy by the vertical motions within the waves – maintaining the kinetic energy of the atmosphere against frictional dissipation. The waves intensify until the heat transported northward balances the radiation deficit. Various processes (friction, thermal

conductivity, radiation to space, etc.) damp the waves and the baroclinic process is eventually repeated, albeit in a very asymmetric manner.

While these unstable planetary waves have waxed and waned (observed as 4-7 large scale meanders of the jet stream around a hemisphere) atmospheric scientists have not found repeatable patterns – except in the southern hemisphere where a "vacillation" period of approximately 23 days has been sometimes observed. No such vacillation has been consistently identified in the northern hemisphere—presumably because of the more heterogeneous pattern of continental mountain ranges and oceans.

Every general circulation model of the global atmosphere, weather prediction model, and climate prediction model has the necessary elements of baroclinic instability embedded within their equations. Numerous authors have contributed texts and articles on linear stability analysis of baroclinic waves. A partial list of early important work would include Lorenz (1963), Pedlosky and Frenzen (1980), Hart (1981), and Pedlosky and Polvani (1987). The nonlinear nature of the baroclinic process leads to a variety of phenomena: fixed point solutions, vacillation, limit cycles, and chaos. Thompson's (1987,1988) low order general circulation model exhibited the vacillation period seen in the southern hemisphere with the period very close to the 23 day period seen by Webster, et al (1975). Fleming (2014), hereafter referred to as F14, used this model to identify explosive baroclinic instability which occurs with varying initial conditions.

The atmosphere occasionally exhibits this explosive baroclinic instability. An example that occurs in the late fall or early winter is the extremely cold Arctic air that is driven southward deep into Mexico. Another example occurs in the late spring or early summer when warm moist air is driven northward deep into Canada. Such events may occur perhaps only a few times a year and not every year with the same duration nor same intensity. When they occur, the result is profound. In 2014 such an event caused a new low temperature record for Denver, CO on November 12, breaking a 132 year old record of -4 F set in 1882; a few days later that same system (November 17-19) gave Buffalo, NY its epic lake-effect snow of over 5 feet of snow. The extensive arctic air that covered the USA in the winter of 2015 set all-time records for February snowfall in both Boulder, CO in the Midwest and in Boston, MA in the East.

Monte Carlo methods are discussed in many references, consider Gilks et al. (1996) for details and references. The stochastic dynamic equations are much less known and references are found in Chapter 2. This chapter will explain the mathematical approach of **combining** stochastic dynamic equations with MC calculations. The power of the MC method is its ease in programming for parallel processing computers. When MC calculations are combined with the **analytical use** of the stochastic dynamic equations, a powerful tool for analyzing nonlinear systems is available.

Chapters 3 and 4 provide a tutorial on how to use the combined approach for looking deeper into nonlinear systems like the relatively simple Lorenz and Rössler strange attractors. The Lorenz attractor in Chapter 3 (Lorenz, 1963) has been well studied, but new relationships among the variables are revealed. The Rössler attractor in Chapter 4 (Rössler, 1976), on the surface seems quite uninteresting, but what happens when the non-attracting second fixed point is explored by the SDE/MC approach is rather amazing.

Chapter 5 reviews key points about the large scale attractor associated with the atmosphere's explosive baroclinic instability. This was introduced in F14. This attractor is far different from those of Lorenz and Rössler – the spatial scale is hemispheric and the time scale ranges from a few to several weeks. This chapter will add new information about the initial condition dependence on the model solution being a fixed point, a limit cycle, or a chaotic solution. Details on the limit cycle solutions are revealed as this solution exists, in such a perfectly symmetric manner, in such a complicated dynamic system. These **deterministic solutions** will be summarized over the range of differential heating values **(H)** and friction values **(D)** reasonably expected over past and future atmospheric conditions. There is also a discussion of the fractal dimension of the attractor.

Chapter 6 will apply the **combined SDE/MC mathematic approach** to the explosive baroclinic instability (EBI) attractor. This chapter will demonstrate the tremendous diversity inherent in the atmosphere with this explosive baroclinic instability. Other topics include the moment relationships between the variables, the accuracy of the combined approach, the skewness and kurtosis of third and fourth moments, and other topics. There is another rare solution—a chaos solution so violent that it destroys itself and collapses to a fixed point solution.

Why this occurs is explained. Another subject explored in this chapter is the apparent nonlinear feedback inherent in the stochastic dynamic equations.

Chapter 7 reveals several outcomes of this study that can perhaps be used to improve the utility of extended range weather forecasts out to several weeks. While baroclinic instability is the **primary driver** in the atmosphere's motion, there are other modes of variability: suspected seasonal ocean/atmosphere oscillations in the Arctic region, annual Monsoon systems which undergo vacillation in intensity and timing, and interannual phenomena associated with east –west ocean/atmosphere modes in the tropics. A proper model could evaluate these features of the Earth's atmosphere in a more specific way.

Chapter 8 points out another direction for climate modeling. deMenocal (2001) notes that global cooling is generally associated with a collapse of civilizations whereas global warming is associated with great advances in civilizations. The statistical record does not support carbon dioxide as a cause of global warming. A sound scientific basis for this is summarized from the recent book of Sorokhkin, et al. (2007). A summary of the major ice ages in Earth's history, and the glacial and interglacial periods in our present ice age is presented with references from Plimer (2009). The role of explosive baroclinic instability in the asymmetric build-up and decay of the ice sheets is postulated in this chapter. A crude estimate is provided of the timing of this process in a particular example with a 70,000 year cold temperature anomaly as was evident in the Laurentide Ice Sheet.

Chapter 9 returns to the SDE/MC approach with two further applications for addressing nonlinear systems. This includes converting the usual linear term of a constant times a variable, where the constant has uncertainty, into a stochastic quadratic term. A second extension is the stochastic equation set for the n-th moment about the mean when the original deterministic equation is nonlinear and **cubic** in form. These additional tools complete the picture of possible nonlinear feedbacks that may be required for various complex modeling problems that arise in some new fields of biology, chemistry, and sophisticated uses of very large data bases.

Chapter 10 provides a summary of the key findings and some encouraging remarks for the expanded use of the SDE/MC approach in a variety of applications.

Chapter 2

Stochastic dynamic equations and Monte Carlo combined

The mean of any collection of variables X(j) where j = 1 to N is simply the average of those variables – the values summed and divided by N – expressed as the mean of X {$\mu(X)$}. The variance of such a variable is the second moment about the mean and given by the sum of the terms {$[X(j) - \mu(X)]^2$}, then dividing that sum by N. The term "moment" in this study will always be "moment about the mean".

The second moment equations for a dynamic system with quadratic nonlinear terms were introduced to the atmospheric community by Epstein (1969). The general form for a time derivative of a deterministic equation set of X_i variables with nonlinear terms summed over the pair of indices p,q and linear terms summed over the index p, is given by:

$$\partial X_i / \partial t = \sum a_{ipq} \, Xp \, Xq - \sum b_{ip} \, Xp + c_i$$

The first two corresponding moment equations for the means (μ_i) and the second moments about the mean – variance if σ_{jj} and covariance if σ_{ij} are provided below:

$$\partial \mu_i / \partial t = \sum a_{ipq} (\mu_p \, \mu_q + \sigma_{pq}) - \sum b_{ip} \, \mu_p + c_i$$

$$\partial \sigma_{ij} / \partial t = \sum a_{ipq} (\mu_p \, \sigma_{jq} + \mu_q \, \sigma_{jp} + T_{jpq}) + a_{jpq} (\mu_p \, \sigma_{iq} + \mu_q \, \sigma_{ip} + T_{ipq}) - \sum (b_{ip} \, \sigma_{jp} + b_{jp} \, \sigma_{ip}),$$

where T is a third moment about the mean.

The system of equations is not closed as the 2nd moment involves 3rd moments, the third moment equations involve 4th, etc.

The third moment equations were derived and discussed by Fleming (1971a) but are reproduced here in a much simpler form by ignoring the linear terms and just considering a single nonlinear quadratic term (extensions to more terms simply involves permuting the dummy indices):

$$\partial T(j, k, l) / \partial t = a_{jpq} \, [\mu(p) \, T(k,l,q) + \mu(q) \, T(k,l,p) - \sigma(p,q) \, \sigma(k,l) + \lambda(p,q,k,l)]$$
$$+ a_{kpq} \, [\mu(p) \, T(j,l,q) + \mu(q) \, T(j,l,p) - \sigma(p,q) \, \sigma(j,l) + \lambda(p,q,j,l)]$$
$$+ a_{lpq} \, [\mu(p) \, T(j,k,q) + \mu(q) \, T(j,k,p) - \sigma(p,q) \, \sigma(j,k) + \lambda(p,q,j,k)]$$

One can look at error growth due to the uncertainty in the initial conditions of a model with these stochastic dynamic equations, but only for simple systems, as the number of equations involved becomes substantial. The closure issue must be addressed in some manner, (this is briefly discussed in Chapter 6) but that is another topic – not required for this study as the integration of these equations over time is **not required nor desired in this study**.

The author did integrate these equations for a triad of waves interacting with each other and with the zonal flow in a 28-variable model and found that the error growth was primarily driven by the baroclinic instability mechanism (Fleming, 1971 a, b). However, the value of these equations lies not in their actual integration, but in **their completely analytical form with no assumption on closure!** This is discussed shortly, but first one must simplify the notation even further as higher order moments other than 3rd will be dealt with.

Consider the symbol $\mathbf{f_n}$ to be the n-th moment about the mean (where n = 1 is the 1st moment about the mean which (from basic statistics) is = 0 by definition. The symbols of the higher moments will be: n = 2 = σ for the 2nd moments, n = 3 = T for the 3rd moments, n = 4 = λ for the 4th moments, and f_n for the n-th moment.

The simplification below will consider a single nonlinear term (a product of two deterministic variables -- a quadratic form.) Observing the deterministic equations above one can see that the indices are just dummy indexes and that they are all cyclically replaced in the stochastic moment terms and can be added to the individual terms later. The prognostic equation for the **n-th moment about the mean** can be shown to be (the proof is provided in Appendix 1):

$$\mathbf{\partial f_n / \partial t = n [2 \mu f_n - f_2 f_{n-1} + f_{n+1}] \quad for\ n = 2,3 \ldots N} \qquad \mathbf{(1)}$$

The equation for the mean of X is: $\mathbf{\partial \mu / \partial t = \mu \mu + \sigma = \mu \mu + f_2}$

The equations for 2nd moment through the 4-th moments about the mean are:

$$\partial f_2 / \partial t = 2 [\mu f_2 + \mu f_2 + f_3]$$

$$\partial f_3 / \partial t = 3 [\mu f_3 + \mu f_3 - f_2 f_2 + f_4]$$

$$\partial f_4 / \partial t = 4 [\mu f_4 + \mu f_4 - f_2 f_3 + f_5]$$

The prognostic equation for an n-th moment about the mean involves a sum of only three different types of products of moment terms, each of which has the moment product of n + 1. All other potential products of moment terms cancel out as shown in the proof of Appendix 1.

The above nomenclature is undoubtedly too vague for those not yet accustomed to these equations. Therefore, before going into the Monte Carlo method, let us jump ahead and illustrate these equations for the famous three equations of Lorenz (1963) which led to the first well publicized strange attractor.

This attractor and its physical basis will be discussed with the combined SDE/MC approach in Chapter 3. Here we indicate the equations and the chaotic attractor as shown in Figs. 1

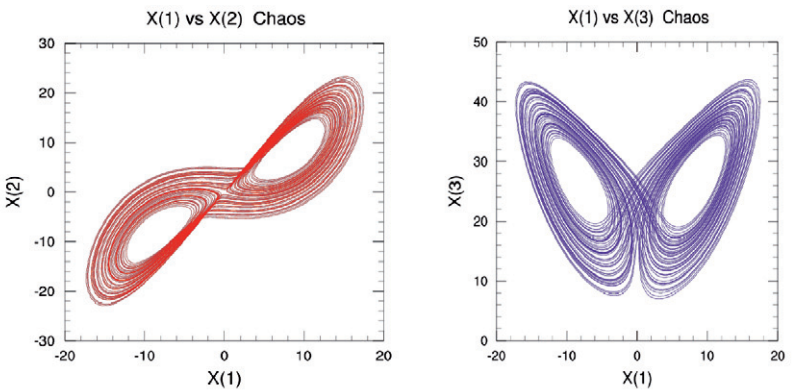

Fig 1. The Lorenz chaotic attractor: X(1) vs X(2) on left vs X(3) on right

[Lorenz uses X,Y and Z for his three dependent variables, but in this study the deterministic dependent variables will be the numerical values X(1), X(2) and X(3). These deterministic equations are:

$$\partial X(1)/\partial t = P\,[X(2) - X(1)]$$

$$\partial X(2)/\partial t = -X(1)\,X(3) + R\,X(1) - X(2) \qquad \textbf{(2)}$$

$$\partial X(3)/\partial t = X(1)\,X(2) - B\,X(3)$$

where the constants P, R and B are discussed later; R = 28 gives the chaotic solution.

The stochastic dynamic equations for the means and a few of the 2nd moments are illustrated below:

$\partial\, \mu(1)/ \partial t = P\, [\mu(2) - \mu(1)]$

$\partial\, \mu(2)/ \partial t = -[\mu(1)\, \mu(3) + \sigma(1,3)] + R\, \mu(1) - \mu(2)$

$\partial\, \mu(3)/ \partial t = \mu(1)\, \mu(2) + \sigma(1,2) - B\, \mu(3)$

$\partial\, \sigma(1,1) /\partial t = 2P\, [\sigma(1,2) - \sigma(1,1)]$

$\partial\, \sigma(1,2)/ \partial t = P\, [\sigma(2,2) - \sigma(1,2)] - [\mu(1)\, \sigma(1,3) + \mu(3)\, \sigma(1,1) + T(1,1,3)] + R\, \sigma(1,1) - \sigma(1,2)$

$\partial\, \sigma(1,3) /\partial t = P\, [\sigma(2,3) - \sigma(1,3)] + [\mu(1)\, \sigma(1,2) + \mu(2)\, \sigma(1,1) + T(1,1,2)] - B\, \sigma(1,3)$

$\partial\, \sigma(2,2)/ \partial t = -2\, [\mu(1)\, \sigma(2,3) + \mu(3)\, \sigma(1,2) + T(1,2,3)] + R\, \sigma(1,2) - \sigma(2,2)]$

The trick in quickly determining these second moment prognostic equations [σ(i,j)] is to consider the prognostic equation for the first index (i) and add the second index (j) to the terms encountered on the right hand side of that (i) equation. One is now half done – now consider the prognostic equation of the second index (j) and add the first index (i) to the terms encountered on the right hand side of that (j) equation. When i = j, the second half of the process just repeats the first half and one has a "2" in front of the first half result.

The process is similar for third moment prognostic equations: one starts with a single index and then carries the other two indices along to the terms in the right hand side of that first index equation; then one permutes this effort as above.

The result in Fig. 1 is the strange attractor for this Lorenz system of equations with R= 28. When a system is bounded and dissipative as the Lorenz system, all trajectories eventually tend toward some bounded set of **zero volume in phase space**. The zero volume could be a fixed point, a surface, or a fractal dimension of less than three (for the Lorenz attractor the fractal dimension is 2.02). Knowing this, one can investigate the statistical nature of the attractor by the following process.

First flood the attractor with a great many Monte Carlo initial states – each taken from a random number generator with deviates drawn from a normal distribution about the starting point for the initial condition which produced the attractor solution. For Fig.1 the initial conditions were (0, 1, 0) for X(1) through X(3). Integrate these initial conditions for an extremely long time, then average these MC results over a suitably long time such that the statistics are stable – the system is ergodic. The MC results can then be used to calculate all the higher order moments one feels necessary to understand the attractor. **These will simply be numbers with little apparent value.**

If all has been carried out as described above, the power of the combined method here is that the **time averaged Monte Carlo moments will agree exactly with relationships described by the left hand side of the full stochastic dynamic equations set to zero.** No assumption on the closure of the equations is required. The MC results, by themselves just numbers, now provide powerful information by being combined with the stochastic dynamic equations (SDE).

The stochastic equations (with the left hand side set to zero) give precise equations or relationships among the various moment terms. This reveals precise numerical relationships among the moments which are not evident from a visual inspection of the attractor itself.

The first use of this combined approach (though it was not referred to in this manner) was in Fleming (1993) where a study of MC sample size versus averaging time was conducted using the time variance of a 3rd moment as a guide. The MC sample size of 10,000 or greater is now preferred. Time integrations with time averaging over 60 times the "typical" chaotic period is important. The Lorenz model had "typical" chaotic periods of 70 iterations.

There are various ways one can compute the MC results. One way which is both fast, systematic and logical, and saves memory space is briefly described in FORTRAN code in Appendix 2.

The combined approach described above will be referred to as the SDE/MC approach where the SDE portion will be the full stochastic dynamic equations as defined by **(1**) up to the prognostic equation for the n-th moment, and with the n+1 term included on the right hand side with no assumptions on closure.

Chapter 3

The SDE/MC approach on the original Lorenz attractor

The Lorenz equations given by **(2)** represent a simplified model of fluid convection in the X-Z plane with the fluid heated from below and cooled from above.

Lorenz's X: X(1) used here, is proportional to convective overturning; his Y: X(2) used here, measures the horizontal temperature variation between currents; and his Z: X(3) used here, measures the distortion of the vertical profile from linearity. The constants in **(1)** and used in all results for this chapter are: P = Prandtl number = 10; B = ratio of horizontal wavelength to depth of the fluid = 8/3; and R = Rayleigh number = 28. Lorenz (1963) found that for R < 1 there was no convection, for R > 1 there were two additional steady state solutions $X(1) = X(2) = \pm [B (R-1)]^{\frac{1}{2}}$, $X(3) = R -1$.

The above steady state become unstable when $R = P (P+B+3)/ (P-B-1) = 24.74$. When the initial conditions are (0,1,0), R = 14 produces the solution $X(1) = X(2) = -[B (R-1)]^{1/2} = -[8/3 (14 -1)]^{1/2} = - 5.888$ and $X(3) = R-1 = 13$.

With the same initial conditions and R = 28, the strange attractor seen in Fig.1 is for iterations 8,000 to 16,000 – which quite easily removes the influence of the initial transition phase. The essential properties for a strange attractor are: (i) phase trajectories are attracted toward it, (ii) pairs of close neighboring trajectories diverge on it (this is called sensitivity to initial conditions, and (iii) it has a fractal dimension.

A unique attribute of a strange attractor is that the trajectory does not intersect itself if one considers the full three dimensional picture – the apparent crossings in Fig. 1 are due to the projection of the attractor on two dimensions. Many authors have studied the Lorenz attractor, particularly for R = 28. Sparrow (1982) has an entire book dedicated to various values of R.

The MC sample size used here was 40,000 and the time averaging was over the last 4000 iterations of an integration to 16,000. Table 1 indicates the computed MC values and calculated SDE values from the equations with the left hand side set to zero – these are for the 3 mean values, the 6 second moment terms, and the 10 third moment terms. Table 2 presents the same information for the fourth

moment terms, but variables # 30 through #34 are fourth moment terms that are not in the SDE set.

First, an important generalization as pointed out by Sparrow (1982), the Lorenz attractor has a natural symmetry involving X(1) and X(2). Thus, all moments of second and higher that have an odd number of 1's and 2's in the indices will approach zero over time. Thus, one can see in Table 1 that σ(1,3), σ(2,3), T(1,1,1), T(1,1,2), T(1,2,2), T(1,3,3), T(2,2,2), and T(2,3,3) all approach zero in the calculated MC results and are exactly zero in the calculated SDE results.

Variable #	Moment	SDE Value	MC Value	Variable #	Moment	SDE Value	MC Value
1	μ(1)	.000	-.001	10	T(1,1,1)	.000	.060
2	μ(2)	.000	-.001	11	T(1,1,2)	.000	.060
3	μ(3)	23.55	23.55	12	T(1,1,3)	400.6	400.6
4	σ(1,1)	62.8	62.8	13	T(1,2,2)	.000	.040
5	σ(1,2)	62.8	62.8	14	T(1,2,3)	198.24	198.24
6	σ(1,3)	-.000	-.005	15	T(1,3,3)	-.000	-.080
7	σ(2,2)	81.20	81.20	16	T(2,2,2)	.000	.009
8	σ(2,3)	.000	.001	17	T(2,2,3)	84.83	84.83
9	σ(3,3)	74.34	74.34	18	T(2,3,3)	-.000	-.060
				19	T(3,3,3)	132.4	132.4

Table 1. Computed SDE values and calculated MC values for Lorenz eq.

Table 2 also verifies this same result for those λ(i,j,k,l) that have an odd number of 1's and 2's in the indices. One can observe that the calculated results from the SDE match the MC results extremely well – **exact in most cases**, but only off 1 part in 10^5 even in the worst of the non-zero fourth moment results.

Variable #	Moment	SDE Value	MC Value	Variable #	Moment	SDE Value	MC Value
20	λ(1,1,1,1)	9060.1	9060.1	27	λ(1,2,2,3)	0.0	-.15
21	λ(1,1,1,2)	9060.1	9060.2	28	λ(1,2,3,3)	5021.6	5021.5
22	λ(1,1,1,3)	0.0	-.14	29	λ(1,3,3,3)	0.0	-.12
23	λ(1,1,2,2)	10737	10735	30	λ(2,2,2,2)		18789
24	λ(1,1,2,3)	0.0	-.003	31	λ(2,2,2,3)		-.008
25	λ(1,1,3,3)	6711.0	6712.5	32	λ(2,2,3,3)		5354.5
26	λ(1,2,2,2)	13,774	13,774	33	λ(2,3,3,3)		.37
				34	λ(3,3,3,3)		11838

Table 2. Same as Table 1 with the 4th moments (the final five are not in the equation set).

3.1 Relationships from the SDE/MC approach for the Lorenz attractor

Now examine the individual equations and one can find some exact relationships between the moment terms (only a few are evident by observing the attractor).

From ∂ μ(1) /∂t = 0 = P [μ(2) - μ(1)]; one has **μ(1) = μ(2).**

From ∂ μ(2) /∂t = 0 = - μ(1) μ(3) – σ(1,3) + R μ(1) - μ(2); one has μ(1) [μ(3) - R + 1] = 0; but, in the bracket if μ(3) is not equal to R -1 (as with R=14), thus the terms in the bracket are not zero, therefore **μ(1) = 0 and also then μ(2).**

From ∂ σ(1,1) /∂t = 0 = 2P [σ(1,2) – σ(1,1)]; one has **σ(1,1) = σ(1,2)**

and from ∂ μ(3)/ ∂t = 0 = μ(1) μ(2) + σ(1,2) – B μ(3); one has **σ(1,2) = B μ(3).**

Thus**, σ(1,1) = σ(1,2) = B μ(3) = (8/3) (23.55) = 62.8** which agrees exactly with Table 1.

From ∂ σ(3,3) /∂t = 0 = 2 [μ(1) σ(2,3) + μ(2) σ(1,3) + T(1,2,3) – B σ(3,3);

one has **T(1,2,3) = B σ(3,3) = (8/3) (74.34) = 198.2** which agrees exactly with Table 1.

This last result is not obvious – the triple correlation of the three variables being a product of a model parameter with the variance of the key variable X(3). In the above examples, the numerical values of μ(3) and σ(3,3) had to be obtained from the MC results – there were no previous equations that provided these values. A similar requirement for the value of T(3,3,3) was needed to compute λ(1,2,3,3).

A check of two more complicated expressions will verify the accuracy of the SDE/MC approach. Take the time derivative of σ(1,2) to arrive at the third moment T(1,1,3).

From ∂ σ(1,2) /∂t = 0 = P [σ(2,2) – σ(1,2)] – [μ(1) σ(1,3) + μ(3) σ(1,1) + T(1,1,3] +R σ(1,1) – σ(1,2); thus one has:

T(1,1,3) = R σ(1,1) – σ(1,2) - μ(3) σ(1,1) + P σ(2,2) - P σ(1,1); from Table 1:

400.64 = σ(1,1) [R – P – 1 - μ(3)] + P σ(2,2)

400.64 = (62.8) [28 – 10 – 1 – 23.55] + (10) (81.2) = 812 – 411.34 = 400.66

Then take the time derivative of this term: ∂ T(1,1,3) /∂t = 0 = 2P [T(1,2,3) – T(1,1,3)] + μ(1) T(1,1,2) + μ(2) T(1,1,1) – σ(1,2) σ(1,1) + λ(1,1,1,2) – B T(1,1,3)

to arrive at the 4th moment λ(1,1,1,2):

One has**: λ(1,1,1,2) =** (B + 2P) T(1,1,3) -2P T(1,2,3) + σ(1,2) σ(1,1); from Tables 1 and 2:

9060.2 = (8/3 +20) (400.64) – (20) (198.24) + (62.8) (62.8) = 9060.21

One could go on and verify other numerical values, but rather one should illustrate another interesting relationship involving all three variances of the dependent variables.

From ∂ σ(2,2) /∂t = 0 = - 2 [μ(1) σ(2,3) + μ(3) σ(1,2) + T(1,2,3)] + 2 [R σ(1,2) – σ(2,2)]; one has

σ(2,2) = σ(1,1) [R - μ(3)] – T(1,2,3) and using the relationship above

T(1,2,3) = B σ(3,3)

σ(2,2) = σ(1,1) [R - μ(3)] – B σ(3,3)

The first surprise here is that there exists a single relationship involving all three variances of the three dependent variables. The numerical relationship is verified by the results from the individual components listed in Table 1:

σ(2,2) = σ(1,1) [R - μ(3)] – B σ(3,3)

81.20 = (62.8) [28 – 23.55] - (8/3)(74.34) = (62.8) (4.45) - 198.24 = 81.22 ≈ 81.20

It is not a surprise that the variance of X(2) differs from the variance of X(1) – the equation for σ(2,2) is quite more complex. Still, it is somewhat strange that the variables X(1) and X(2) are symmetric over the attractor and their mean values, μ(1) and μ(2), both equal zero. However, a careful look at Fig. 1 does indicate that the variability of X(2) is ever so slightly greater than that of X(1). With the SDE/MC approach one can both determine and quantify that variance relationship exactly.

A second surprise is that σ(2,2) has the largest variance of the three with σ(2,2) = 81.2, σ(3,3) = 74.34 and σ(1,1)= 62.8. However, again a closer inspection of Fig. 1 does reveal this difference – which has been quantified.

3.2 Skewness and Kurtosis associated with the Lorenz attractor

The input of random numbers to the initial conditions for the Lorenz attractor were drawn from a normal distribution. A natural question to ask is what are the statistical distributions of the three variable X(1), X(2) and X(3) – are they still normal? Here there is an examination of the skewness and kurtosis of the third and fourth moments, respectively.

From Table 1 one notes that T(1,1,1) and T(2,2,2) = 0 , thus X(1) and X(2) are not skewed. The "moment coefficient of skewness" (S) is given by:

$S = m_3 / (m_2)^{3/2}$ [m_3 is the 3rd moment and m_2 is the 2nd moment about mean.

The 3rd moment about the mean for X(3) is variable #19 in Table 1: T(3,3,3) = 132.4. Here:

$S_3 = 132.4 / (74.34)^{3/2} = 0.206$. This moment coefficient of skewness (m.c.s.) is positively skewed, skewed to the right, meaning that the right tail of the distribution is longer than the left. However the magnitude (S < 0.5) suggests that X(3) is **not moderately skewed, but only slightly so** – 'modestly' skewed would have S in the range (0.5 < S > 1.0.)

A check of the 5th moment, f(3,3,3,3,3) with this same sample size of 40,000 (averaged over 12,000 to 16,000 iterations) was performed. The m.c.s. in this case using f(3,3,3,3,3) is given by S_5 = f(3,3,3,3,3) / (10) σ(3,3) T(3,3,3) = 42,341 / (10) (74.34) (132.4) = 0.43. Thus, this degree of skewness has increased by a factor of 2 but would still not be considered modestly skewed.

There are further relationships that could be explored, but just consider one more that involves the skewness of X(3). Since the mean values of X(1) and X(2) are zero, X(3) is a key variable. A unique sequence of relationships can be derived from the prognostic equations of σ(3,3), T(3,3,3), λ(3,3,3,3), and f_5 (3,3,3,3,3). These are shown below along with the values that indicate that the SDE and MC provide the same consistent results. The numbers come from the calculated MC values and they are input to the exactly derived SDE equations with the left hand side set to zero. The sequence begins with a relationship shown above:

T(1,2,3) = B σ(3,3)

198.24 = (8/3) (74.34) = 198.24

λ(1,2,3,3) = B T(3,3,3) + σ(1,2) σ(3,3)

5021.5 = (8/3) (132.4) + (62.8) (74.34) = 5021.6

f(1,2,3,3,3) = B λ(3,3,3,3) + σ(1,2) T(3,3,3)

39,874 = (8/3) (11,838) + (62.8) (132.4) = 31,568 + 8315 = 39,883 with a relative error of just 0.002%.

f(1,2,3,3,3,3) = B f(3,3,3,3,3) + σ(1,2) λ(3,3,3,3)

856,356 = (8/3) (42,341) + (62.8) (11,838) = 856,336 with a relative error of just 0.002%.

These relationships are interesting, though perhaps just a mathematical curiosity, as the assignment to a physical meaning for the higher moments is not obvious.

Now look at the subject of **kurtosis for the fourth moment terms in the attractor**. Since X(1) and X(2) are known to be symmetric with zero skewness, and X(3) is known to be approximately symmetric with a slight positive skewness, a question remains about the central statistical peaks of these variables: are they high and sharp or short and broad?

The height and sharpness of the peak relative to the rest of the data is measured by a nondimensional number called kurtosis. Higher values of kurtosis indicate a higher, sharper peak; lower values indicate the opposite – a lower less distinct peak. Another description is that higher kurtosis indicates more of the variability is due to a few extreme differences from the mean, rather than a lot of modest differences from the mean. Yet another good description is "increasing kurtosis is associated with the movement of probability mass from the shoulders of a distribution into its center and tails" (Balanda and MacGillivray, 1988).

The moment coefficient of kurtosis is given by $\mathbf{a_4 = m_4 / (m_2)^2}$ **where** m_4 is the 4^{th} moment about the mean and m_2 is the 2^{nd} moment about the mean. **Excess kurtosis** is defined as

K = a_4 - 3 where the **3** comes from the kurtosis of a **normal distribution which is exactly 3.** Now examine five of the nine non-zero 4^{th} moment terms in Table 2.

For X(1), the 4^{th} moment is λ(1,1,1,1) = 9060.1, a_4 = 9060.1 / $(62.8)^2$ = 2.297, which is < 3 which means it is a platykurtic (flat like the bill of a platypus) distribution. Compared to a normal distribution, its central peak is lower and broader, and its tails are shorter and thinner.

For X(2), the 4th moment is λ(2,2,2,2) = 18789, a_4 = 18789 / $(81.2)^2$ = 2.85, which is < 3 which implies it is also a platykurtic distribution. For X(3) the 4^{th} moment is λ(3,3,3,3) = 11838, a_4 = 11838 / $(74.34)^2$ = 2.142, which is < 3 which means it is also platykurtic.

There are two 4^{th} moment terms that are not platykurtic. One is λ(1,2,3,3) = 5021.5. The normal form for this 4^{th} moment is σ(1,2) σ(3,3) + 2 σ(1,3) σ(2,3) = (62.8) (74.34) + 0 = 4668.6. The factor of 3 is already included so the kurtosis is 5021.5 /4668.6 = 1.08, which is > 1, which implies that this 4^{th} moment is just barely leptokurtic. Compared to a normal distribution, its central peak is higher and sharper, and its tails are longer and fatter.

Another considerably more leptokurtic 4^{th} moment is λ(1,1,3 3) = 6712.5. The normal form for this 4^{th} moment is given by σ(1,1) σ(3,3) + 2 σ(1,3) σ(1,3) = (62.8) (74.34) + 0 = 4668.6. The moment coefficient of kurtosis is 6712.6 / 4668.6 = 1.44, which is considerably > 1.

3.3 Evaluation of the feedback term in SDE

Derivation of the prognostic equation for the n-th order moment is contained in Appendix 1. The procedure produces the term "$– f_2 f_{n-1} + f_{n+1}$"automatically, there are no assumptions. The derivation of the prognostic equation for the 3rd moment: $\partial T(i,j,k)/ \partial t = (\ldots - f_2 f_2 + f_4)$ also has this term which can be found in the references, and also found separately in Appendix 1. The fact that there is a negative sign in front of the first term ($f_2 f_2$) suggests that this term may counteract the impact of the positive second term (f_4) which follows. This is investigated now in the Lorenz attractor and will be examined again in the attractor for explosive baroclinic instability.

The above term will only appear in four of the non-zero 3rd moment terms. For example, $\partial T(1,1,1) /\partial t = 3P [T(1,1,2) – T(1,1,1)] = 0$ and the terms of interest are not even present. The four remaining equations are shown below:

$\partial T(1,1,3) /\partial t = 0$ gives the relation $T(1,1,3) = [2P T(1,2,3) \mathbf{– \sigma(1,1) \sigma(1,2) + \lambda(1,1,1,2)}] /(2P +B)$. From Tables 1 and 2, all the terms above are positive and the left side of Fig. 2 indicates that T(1,1,3) reaches the positive value of 400.6. Thus, the term **– σ(1,1) σ(1,2) does reduce the impact of λ(1,1,1,2).**

$\partial T(1,2,3) /\partial t = 0$ yields the relation: $T(1,2,3) = [P T(2,2,3) + \mu(3) T(1,1,3) + \lambda(1,1,3,3) + R T(1,1,3)$ **– σ(1,2) σ(1,2) + λ(1,1,2,2)** $] /(P + B +1)$. From Table 1 and 2, all the terms above are positive and the right side of Fig 2. indicates that T(1,2,3) reaches a positive value of 198.2. Thus, the term **– σ(1,2) σ(1,2) does reduce the impact of λ(1,1,2,2).**

As above, all the **corresponding terms** in $\partial T(2,2,3)/\partial t$ and $\partial T(3,3,3)/\partial t$ are positive as well. The main point is that the nonlinear feedback is occurring – but so far for only positive terms – with the negative sign in front of the first term providing the negative feedback and reducing the impact of the second term.

The curves in Fig. 2. were used as illustrations. These were actual numerical integrations of the original stochastic dynamic equations with a proper closure scheme. It was capable of **both reproducing that first peak in initial wild randomness** in the moments (due to the randomly chosen initial conditions for all three variables) and **the final steady state of the moments** on the attractor.

That closure scheme was possible to do with the **MC results for the Lorenz equation set**. The symmetry of the Lorenz attractor made the task easier and there may not be a similar approach for other nonlinear systems.

Details are not presented here for two reasons. The first reason is that the closure result was presented in a special oral tribute to the late Edward S. Epstein on 5 February 2014. The presentations for the tribute were not peer reviewed but are available via the internet at Fleming (2014a and 2014b). Details on the closure would detract from the author's primary objective in this study.

That brings up the second reason. The full integration of the sde equations, even for a small problem, is **never practical**. What is extremely practical is the method of the SDE/MC approach as outlined in this study which can be incorporated in many applications in the physical sciences, in chemical/biological modeling, and in the area of analyzing large data sets in search of specific outcomes.

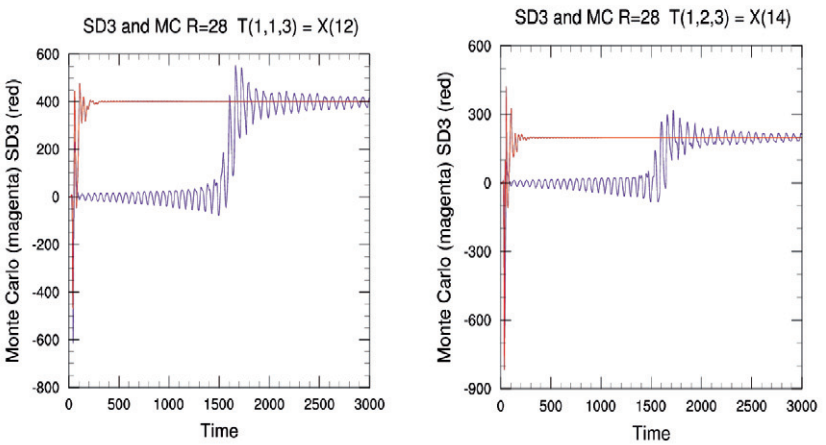

Fig. 2. Direct integration of the SDE set with a proper closure (see text for details). The eventual linear upper curve is the SDE calculation. The lower curve which moves up after 1500 iterations is the MC calculation. Black and white does not indicate how well the first extreme negative values match for both calculations.

Chapter 4

The SDE/MC approach on the Rössler attractor

The Rössler attractor is the attractor for the system of three nonlinear ordinary differential equations that were studied by Otto Rössler (1976). The Rössler attractor is simpler than the Lorenz attractor; it also two fixed points, but one is extremely more attractive than the other. The deterministic eqs. for the attractor [putting X, Y, Z into the numerical form X(1), X(2), and X(3)] are listed below, along with the sde eq. for the means alongside:

$$\partial X(1)/\partial t = -X(2) - X(3) \qquad \partial \mu(1)/\partial t = -\mu(2) - \mu(3)$$

$$\partial X(2)/\partial t = X(1) + a\,X(2) \qquad \partial \mu(2)/\partial t = \mu(1) + a\,\mu(2) \qquad \textbf{(3)}$$

$$\partial X(3)/\partial t = b + X(3)\,[X(1) - c] \qquad \partial \mu(3)/\partial t = b + \mu(3)\,\mu(1) + \sigma(1,3) - c\,\mu(3)$$

The values for the parameters first studied by Rössler (1976) were a = b = 0.2 and c = 5.7. Fig. 3 indicates the attractor with the above parameters with the initial condition on the X's being (1.0, 1.0, 1.0). The fixed points can be found by setting the above time derivatives to zero. The strongly attracting fixed point (0, 0, 0) is at the center of the attractor – clearly seen on the left.

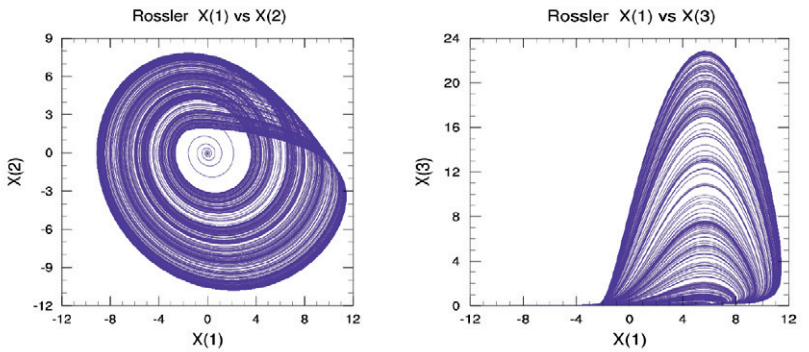

Fig. 3. Rössler attractor X(1) vs X(2) and X(1) vs x(3) with parameters a = b = 0.2 and c = 5.7

The fact that the Rössler attractor is a "strange" attractor can be seen in the first return map shown on the left side of Fig. 4. This plots the sequence of maximum values of X(3) when they occur as the time integration proceeds – producing N maximum values. The value of max X(3) at "n" is plotted along the abscissa and the value of max X(3) at "n+1" on the ordinate. The result is a perfect plot of this predictability feature of a chaotic strange attractor – knowledge of one maximum point determines the relative value of the following maximum point – indicating that there is some *order* within the trajectories of the attractor. This was also found by Lorenz (1963) and will be found in Chapter 6 for the atmosphere's baroclinic strange attractor.

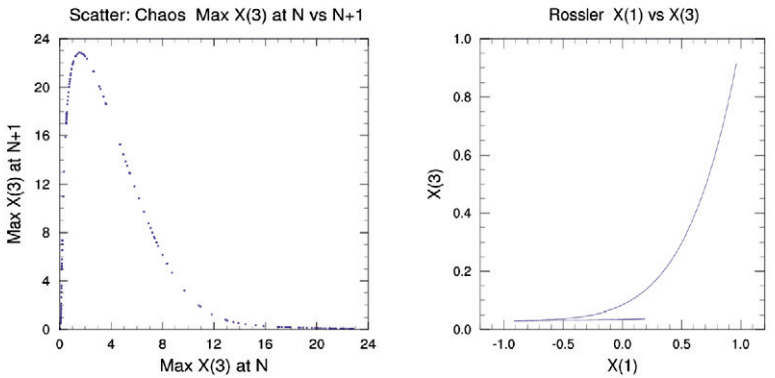

Fig. 4. Rössler attractor: (left) First return map showing consecutive maximum values of X(3). The (right) side is a MC run with X(3) converging to its predicted value (see text).

The Monte Carlo run with this attractor, with 1000 random points, covers the attractor to the extent that the values for the ensemble mean for X(1) and X2) quickly average to zero -- as they circle the fixed point at the origin. Then with $\mu(1)$ converging to zero, the right hand side of the eq. for $\partial\mu(3)/\partial t$ becomes $\mu(3) = b/c = 0.2/5.7 = 3.50877 \times 10^{-2}$. These results are seen in the right side of Fig. 4. This figure has only 2000 iterations, but as $\mu(3)$ approaches its constant value, the

last 1500 iterations for μ(1) are merely plotted over previous μ(1) values; μ(1) is merely getting smaller and smaller as it rotates between "+" and " – " values on an approximate 393 iteration cycle.

It may not seem worthwhile to use this simple Rössler attractor at this stage, but it does show that the MC results are exactly like the sde equations – all MC moments go to zero as predicted by the equations, and the SDE/MC result gives the correct value for the constant for μ(3).

A far more interesting situation occurs when the initial conditions are near the second fixed point. The location of this point is based upon the model parameters (a, b, and c) with the term $[c^2 - 4\ a\ b]^{1/2} = 5.686$ having an important role. The X, Y, and Z coordinates are given by {[c + 5.686)/2], [-c – 5.686]/ 0.4], and [c + 5.686]/ 0.4]} which are [5.693, - 28.465, and 28.465].

The history from others who have examined this second fixed point is that it is unstable, producing extra gyrations, but eventually the trajectory is attracted toward the first fixed point and its attractor. If the initial state of a run is set exactly on these coordinates, nothing happens – it is a fixed point and the trajectory does not move. One can start initial conditions close to the second fixed point and obtain the solution seen in Fig 5. It doesn't take long for the attractive power of the first fixed point to win the day and the trajectory returns to (0, 0, 0).

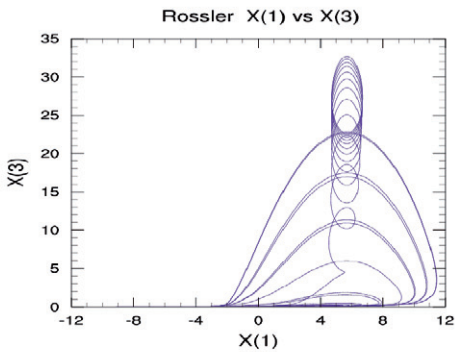

Figure 5. Rössler trajectory after initial condition near the unstable 2nd fixed point

As a final test, the Monte Carlo approach was used with 1000 random deviates **surrounding this second fixed point**. This produced enormous initial instability, but ultimately the MC solutions still converge to the first fixed point and its attractor. Eventually, the same result for the SDE/MC approach occurs as before (all the relations are valid with the values going to zero --except for the constant term for X(3)) as occurred previously.

The **numerical results** during the initial instability phase are revealed here (they are too violent to plot). All numerical integrations in this study were by a 4^{th} order Runge-Kutta scheme (for this attractor the nondimensional time step was .02). The SDE was 0.01 for the MC deviates.

At iteration 130, $\mu(3)$ was still going up in value and was at 0.12×10^{12}, and its variance **$\sigma(3,3)$** had a local **maximum** of 0.25×10^{19} **(yes, 10 to the 19-th power**). In mathematical terms this was like a nuclear explosion -- the initial variance had gone from 0.1×10^{-3} to 0.25×10^{19} in a mere 130 iterations. The MC numerical integrations remained otherwise stable.

At iteration 147 (17 iterations later), $\mu(3)$ had a **maximum** value of 0.19×10^{12}, and the variance **$\sigma(3,3)$** had a local **minimum** of 0.46×10^{16}. At iteration 164 (another 17 iterations later), $\mu(3)$ had lowered slightly to 0.12×10^{12} and **$\sigma(3,3)$** had a second local **maximum** of 0.22×10^{19}.

This showed that the MC deviates had maximum variability **before and after** the $\mu(3)$ max indicating that the deviates were in phase with each other – the variance temporarily fell three orders of magnitude (from 10^{19} to 10^{16}) while $\mu(3)$ peaked.

Subsequently, the value of $\mu(3)$ fell from its maximum value at iteration 147 by an astounding 13 orders of magnitude in the next 200 iterations. At that point in time, $\mu(3) = 0.69 \times 10^{-1}$, and the variance of X(3) was now 0.14×10^{-5}. Thereafter, $\mu(3)$ went through minor oscillations until it reached its constant value of b/c = 3.50877×10^{-2} – matching the expected MC result.

Chapter 5

Explosive baroclinic instability reviewed and broadened

The MC calculations have survived all the tests. The numerical values from those calculations match the identities and relations indicated by the full stochastic dynamic equations. The study is now ready to apply the SDE/MC approach to explosive baroclinic instability. This atmospheric instability has been recently studied in F14. The details of that purely deterministic effort need not be repeated, but the main issues concerning whether strange attractors, limit cycles, and fixed points occur needs to be strengthened and broadened to include another atmospheric parameter besides the equator-to-pole differential heating term. The additional factor that will contribute to nonlinear attractors in the atmosphere is the effect of friction.

The subject of explosive baroclinic instability is revealed in F14. Only essential information for this study will be repeated here. The equations derived for the low order general circulation model were derived by Thompson (1987, 1988) in his study of vacillation (described and shown below).

The model consisted of a single finite-amplitude baroclinic wave interacting with the zonal mean shear flow, maintained against friction by differential heating. The physical basis for his study was the two-level quasi-geostrophic model for flow in a ß-plane channel, with differential heating and eddy diffusion of heat and momentum. The equations from his second paper were rescaled and used in F14 in the following form:

$$\partial X(1)/\partial t = -L R X(2) - L D X(1) + H$$

$$\partial X(2)/\partial t = X(1) X(3) - D X(2) - R X(4) \qquad \textbf{(4)}$$

$$\partial X(3)/\partial t = X(1) X(2) - D X(3)$$

$$\partial X(4)/\partial t = R X(2) - D X(4),$$

where the constant parameters are: **H = 0.042253, D = 0.202**, L = 0.065, R = 0.5858.

X(1) = the mean zonal shear (or mean horizontal temperature gradient).

X(2) = the net poleward heat transport averaged over a full wavelength in the x-direction.

X(3) = the mean kinetic energy (which always must remain positive in all circumstances).

X(4) = the correlation between temperature and geopotential.

Vacillation implies a steady cycling of the baroclinic growth and decay with a slow decreasing amplitude over time. Thompson's study revealed that all cases of vacillation solutions would eventually lead to fixed point values (solved for by setting the left side of eq. set **(4)** set to zero), and that the period of the vacillation cycle was always the same for a given value of **H** and **D**. His model produced quite accurate results of the mean vertical shear, the meridional velocities at the two levels, and the vacillation period of approximately 23 days – close to that seen in the southern hemisphere (Webster and Keller, 1975). His formula for vacillation periods was found to be proportional to $\mathbf{(D/H)^{1/2}}$ (Thompson, 1988) and was found in F14 and in this study to be accurate for vacillation for a wide range of parameter values.

Setting the time tendencies to zero in equation set **(4)** provides the following set of equations:

$$LR\ X(2)_0 + LD\ X(1)_0 = H \qquad \mathbf{(5)}$$

$$X(1)_0\ X(3)_0 - D\ X(2)_0 - R\ X(4)_0 = 0 \qquad \mathbf{(6)}$$

$$X(1)_0\ X(2)_0 - D\ X(3)_0 = 0 \qquad \mathbf{(7)}$$

$$R\ X(2)_0 - D\ X(4)_0 = 0 \qquad \mathbf{(8)}$$

Here the subscript "zero" denotes an equilibrium or fixed point (FP) value.

Solving for $X(3)_0$ and $X(4)_0$ in eqs. **(7**) and **(8**) and inserting the results in **(6)** yields

$X(3)_0 = X(1)_0\ X(2)_0 / D$ and $X(4)_0 = R\ X(2)_0 / D$ and subsequently:

$$X(2)_0\ [(X(1)_0)^2 - (R^2 + D^2)] = 0 \qquad \mathbf{(9)}$$

The FP values for a given values of **H** and **D** and the constants above are:

$X(1)_0 = (R^2 + \mathbf{D^2})^{1/2}$ (X1FP = 0.61965)

$X(2)_0 = \mathbf{H}/LR - \mathbf{D}\, X(1)_0/R$ (X2FP = 0.89600)

$X(3)_0 = X(1)_0\, X(2)_0 / \mathbf{D}$ (X3FP = 2.74855)

$X(4)_0 = R\, X(2)_0 / \mathbf{D}$ (X4FP = 2.59840).

Equation **(9**) is extremely important as there **are three possible solutions** for this dynamic system that eminent from **(9).** The **first** discussed here is $X(2)_0 = 0$. From the FP values above, if $X(2)_0 = 0$ then also $X(3)_0$ and $X(4)_0 = 0$. This is a condition of zonal flow with only X(1) having the theoretical solution from **(5)** of X(1) = **H** / L D. It was shown in F14 that this zonal solution is unstable and will never likely occur for our atmosphere.

The critical value for **H** to be unstable **is** $\mathbf{H > L\, D\, (R^2 + D^2)^{1/2}}$ – this value with the parameters inserted is $\mathbf{H_{Critical} = 0.00814}$ – which is a factor of **5.2 times smaller** than the differential heating value one sees for today's atmosphere of **H = 0.042253.** This zonal solution (though unstable, and not actually possible, is strongly attractive) and it will come up again in later discussions of chaos and also again in Chapter 6.6.

The second solution to (9) is $\mathbf{X(1) = + (R^2 + D^2)^{1/2}}$ **which leads to vacillation**. This solution is stable and proof of that is shown in Appendix 3. The different solutions that are possible with this FP value of X(1) are: a fixed point attractor (though not as powerful as one of the Rössler fixed points), several limit cycle attractors (that are parameter, i.e., **H** and **D**, dependent), and a chaotic attractor **(that is initial condition dependent).** Each is discussed in due time.

Thompson did not discuss chaos in his papers and obviously did not run a set of initial conditions that would produce chaos. However as seen in F14, the choice of initial conditions to run this model can lead to **either vacillation or chaotic solutions**. For any initial state that does lead to vacillation, that period of vacillation is the same for all such initial states and the trajectory is attracted to the same fixed point for all such states. Those FP values were identified above. An example of a vacillation solution is shown in the left side of Fig. 6. Here the vacillation period is 1942 iterations (25.2 days) – with a starting value of **X(1) = 67% of its fixed point value.**

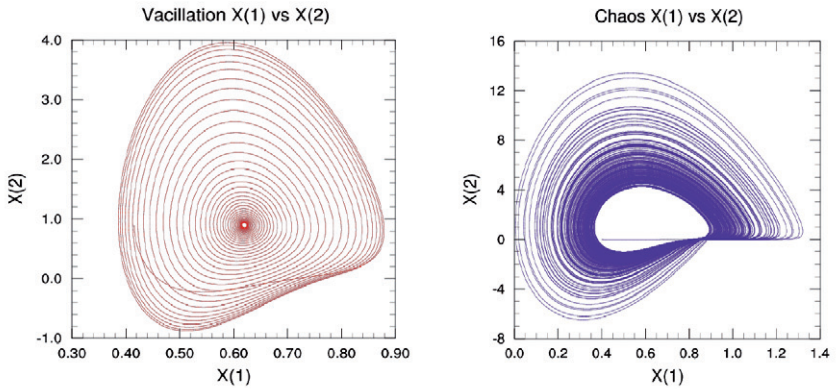

Fig. 6. Vacillation on the left and chaos on the right. (Note significant scale change.)

An example of chaos for an initial state **chosen extremely close to the above state** (same values for all the variables except **X(1) = 66% of its fixed point value**) is shown on the right side of Fig. 6. The chaos cycles have periods which vary considerably from cycle to cycle (and for different initial states); here the largest cycle is 2695 iterations.

The most important distinction between vacillation on the left and chaos on the right is the scale difference, the range of X(1) and X(2) is approximately three times greater for the chaos case – the complete trajectory of the vacillation solution nearly fits inside the open space of the chaos trajectory. When such a great difference occurs from two closely spaced points, this is **explosive baroclinic instability.**

The third possible solution to equation (9) is $X(1) = -(R^2 + D^2)^{1/2}$. This solution is unstable as also shown in Appendix 3. It is not only unstable, but would give non-physical results if achieved —the kinetic energy term X(3) could become negative, but the dynamic system avoids this. It is nevertheless attractive and it will come up again in the context of maintaining numerically stable conditions for all possible computational runs. This is discussed in Chapter 6.

5.1 Chaos and Limit Cycles

Unless otherwise stated, the differential heating used here is that thought by Thompson to be applicable for typical equator-to-pole differential heating in today's world. This value of **H** (defined above) will be referred to as **(1.0) H** as the norm and then changed in subsequent runs where the coefficient will vary **from (0.55) H to (1.3) H.** The friction parameter **D** (defined above as **D = .202**) was also thought to be a typical value – though this value is not precisely known and probably not a true constant – nor is **H which certainly changes with the seasons of the year** . These values of **H** and **D** were used in Fig. 6 above and in Fig. 7 below.

A fair amount of analysis was required to determine when explosive chaos occurred versus the more casual waxing and waning of the baroclinic cycle usually seen in the atmosphere. Be aware that in the real atmosphere, because of land/ocean contrasts and many nonlinear processes associated with small scale effects, the vacillation itself may be constantly changing – new periods may occur before those attractive FP values are reached.

The approach used here was to obtain the exact values of the roots of the characteristic equation, the eigenvalues, of the perturbation equation of the model (see F14 for details). This is the approach used by Lorenz and many others. The analysis is performed, not just at equilibrium points, but at every time step of the trajectory of the dynamic system through phase space – providing a detailed look at baroclinic instability in all its phases of growth and decay.

This is mathematically similar to obtaining Lyaponov exponents at each time step. However the maximum Lyaponov exponent for stability is not sufficient for this baroclinic study as there is a critical eigenvalue that must be exceeded for chaos to occur. The eigenvalues, driven by the variables themselves, are in the form of either: **a single real root and two complex conjugate roots,** (the ultimate form for vacillation to occur) or in the form of **three real roots R1, R2, and R3**. In this latter case, the three real roots may temporarily occur, then disappear with vacillation. The root R1 is usually large negative. R3 is always quite small and usually negative. The root R2 is always positive when it occurs with the other real roots, but chaos only occurs if the **R2 root exceeds its critical value** which is a function of **H** and **D**. In F14 the critical values for R2 as a function of **H** were determined.

There is no way of knowing *a priori* which initial state will produce chaos. But a great deal of information has been gathered.

In F14 it was stated that the initial condition dependence producing chaos was a quite complicated function of X(1), X(2) and X(3). Only a discussion of the root structure during the baroclinic cycle was used to illustrate the chaos formation.

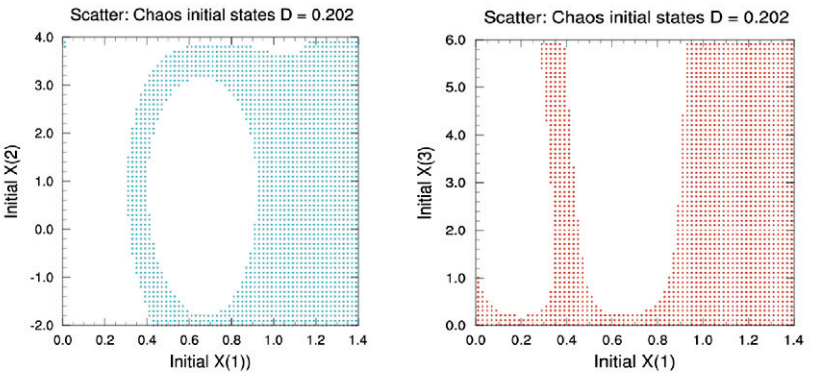

Fig. 7. Initial states that produce chaos: (left) in X(1) - X(2) plane, X(3) = 4.0 for all runs; (right) in X(1) - X(3) plane, X(2) = 0.0 for all runs. Initial conditions chosen for the SDE/MC approach were chosen from the right side with (0.4, 0.0, 0.25, 0.25) – see text.

A better way of **illustrating chaos,** as a function of initial conditions, is with Fig. 7. The left side of Fig. 7 shows those initial states in the X(1) – X(2) plane that lead to chaos. **Here X(3) = 4.0** for all runs.

All calculations in this Section were performed with a time step of 0.01. The right side of Fig. 7 indicates those initial states in the X(1) – X(3) plane that lead to chaos. **Here X(2) = 0.0** for all runs. [X(4) has no influence of the stability of the system -- its role is discussed in a later chapter.]

There are two critical parameters, **H** and **D** that lead to a host of attractors for this model: the fixed point attractor which is the ultimate destination of a vacillation cycle, several period -Limit cycle attractors as intermediate entities, and the

strange attractor for chaos. One need not consider values of **H** and **D** beyond what one might reasonably expect for the Earth's atmosphere over time. Between glacial and inter-glacial periods one could expect some modest changes in **H** and perhaps some accompanying less modest changes in **D**. In the examination of the power of these two parameters to drive different solutions, the range will be restricted to reasonable values of the parameters.

In order to reveal the nature of the impact of these parameters **H** and **D** driving solutions to the various attractors, a **single** initial state is chosen. That state will be one that produces chaos with the parameters valid for our current atmosphere: **H = (1.0) H** and **D = 0.202**.

From the right side of Fig 7, that value chosen for the impact study of **H** and **D**, and for the initial state for the SDE/MC approach was: X(1) = 0.4, X(2) = 0.0, X(3) = X(4) = 0.25. This point is in the left region of chaos in the right side of Fig. 7.

This chaos run produces the chaotic attractor result shown on the left side of Fig. 8 with X(1) plotted versus the R1 root. The strong negative correlation between R1 and X(1) is quite evident.

The right side of Fig. 8 is also the chaos run from these same initial conditions and indicates X(1) versus the positive R2 root. It is clear that R2 leads X(1), but then goes to zero before reappearing later in the cycle as discussed in F14.

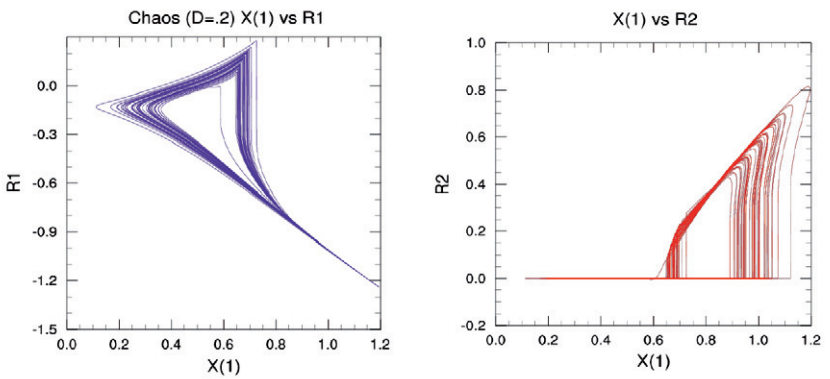

Fig. 8. Chaos run with X(1) vs R1 on the left and X(1) vs R2 on the right

The above initial condition is used for **all** the runs that follow to produce Table 3.

H /D	.55	.60	.65	.70	.75	.80	.85	.90	.95	1.0	1.05	1.10	1.15	1.20	1.25	1.3
.30	F	F	F	F	F	F	F	F	F	F	F	F	F	F	F	F
.29	F	F	F	F	F	F	F	F	F	F	F	F	F	F	F	F
.28	F	F	F	F	F	F	F	F	F	F	F	F	F	F	F	F
.27	F	F	F	F	F	F	F	F	F	F	F	F	F	F	F	F
.26	F	F	F	F	F	F	F	F	F	F	F	F	F	F	F	F
.25	F	F	F	F	F	F	F	F	F	F	F	F	F	F	F	F
.24	F	F	F	F	F	F	F	F	F	F	F	F	F	F	F	F
.23	F	F	F	F	F	F	F	F	F	F	F	F	F	F	C	C
.22	F	F	F	F	F	F	F	F	F	F	F	F	C	C	C	C
.21	F	F	F	F	F	F	F	F	F	C	C	C	C	C	C	C
.20	F	F	F	F	F	F	F	F	C	C	C	C	C	C	C	C
.19	F	F	F	F	F	F	C	C	C	C	C	C	C	C	C	C
.18.	F	F	F	F	C	C	C	C	C	C	C	C	C	C	L_4	L_2
.17	F	C	C	C	C	C	C	L_3	C	C	C	L_2	C	C	C	L_2
.16	F	C	C	C	C	C	C	C	L	C	C	L_4	L_2	L_2	L_2	L_2
.15	F	C	C	C	L_4	L_4	L_4	L_4	L_4	L_2	L_2	L_2	L_2	L_1	L_1	L_1
.14	F	C	C	L_2	L_2	L_2	L_2	L_2	L_2	L_1	L_1	L_1	L_1	L_1	L_1	L_1
.13	F	F	C	L_2	L_2	L_2	L_1	L_1	L_1	L_1	L_1	L_1	L_1	L_1	L_1	L_1
.12	F	F	L_1	L_1	L_1	L_1	L_1	L_1	L_1	L_1	L_1	L_1	L_1	L_1	L_1	L_1
.11	F	F	F	L_1	L_1	L_1	L_1	L_1	L_1	L_1	L_1	L_1	L_1	L_1	L_1	L_1
.10	F	F	F	F	F	L_1	L_1	L_1	L_1	L_1	L_1	L_1	L_1	L_1	L_1	L_1

Table 3. Solutions for H from (0.55) H to (1.3) H and values of D from 0.10 to 0.30. The F = Fixed point, C = Chaotic solution, L = Limit cycle solution (subscripts on L = 1, 2, or 4 - period Limit cycle).

Before going into the details of Table 3, it is worth reviewing results from F14 that dealt with **H beyond** the practical limits shown in Table 3. For **H = (4.0) H to (3.56) H** there is no chaos – only vacillation. As **H** decreases just below the value of **(3.56) H** the solutions can be a fixed point or a single-period limit cycle – the latter occurring if the R2 root is greater than its critical value. With further decrease in **H**, the unstable solution occurs as a sequence of period doubling with two -, four - , and eight-period limit cycles. When H decreases to the value **(1.92) H** the only solutions are fixed point and chaos – with chaos occurring only when the critical value of R2 (itself a function of **H**) is exceeded.

This route to chaos is exactly as described by Berge, et al (1984) stated as **subharmonic cascade**. There is a sequence of periodic attractors, separated by subharmonic bifurcations each of which doubles the number of points on the attractor, as well as its period. The value of **D = .202** was used in F14 and that result is reflected in the middle of Table 3 with **D = 0.20**. If one follows that same line of **D = 0.20** toward the left of the Table with smaller values of **H**, one sees that there is no chaos for values of **H ≤ 0.90**.

The exit from the unstable chaos regime to pure fixed point solutions is also a process of **inverse cascade** where the final entity (before entering the stable regime of only vacillation) is the single-period limit cycle. This is not observed in Table 3 for **D = .20** because the **ΔH** is too large, but is seen in the lower portion of Table 3 for the smaller values of **D**. In general one would observe greater complexity as one descends down to smaller values of **H** and **D** if the **ΔH** and **ΔD** were significantly smaller – but that detail does not serve the purpose of this study. That complexity in the fine structure as the friction parameter decreases was seen in the study of Pedlosky and Polvani (1987).

The driver for chaos is the battle between the real roots R1 and R2. One can observe this battle as a function of **H** and **D** as the discussion now centers on the results of Table 3.

The big picture is that for large **H** and small **D** there exists a very fast system – large forcing and minimal dissipation – **this is the lower right corner of Table 3**. Here the attractors are limit cycles – primarily single-period limit cycles. These are unique and discussed shortly.

The upper left corner of Table 3 has small **H** and large dissipation **D** which is a very sluggish system – small forcing and large dissipation. For large dissipation **(D ≥ 0.24)** there is only a stable dynamic system with only fixed point solutions possible – no chaos. The single-period limit cycle attractors are quite interesting. These are unique and discussed shortly. An image of a typical limit cycle is shown on the left side of Fig. 9

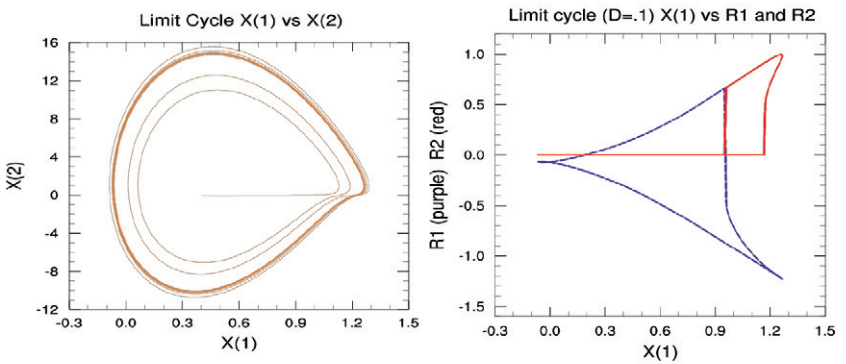

Fig. 9. (Left side) A typical Limit cycle with X(1) vs X(2). (Right side) the change in the root structure during a Limit cycle with X(1) versus the R1 root (purple dashed line) and the R2 root (red line).

Within any cycle the maximum value of the four variables repeat with the **exact** same period and maintain the **same phase relationship** to each other – and with the **same phase relationship relative to that of the R2 root**. The change in the root structure during a limit cycle occurs like it does in the chaos cycle shown in Fig. 8. However, the shape of the root structure is quite different as seen in the right hand side of Fig. 9. Note the orderly, near linear structure on the right side of Fig. 9 versus the chaotic nature in Fig. 8.

The maximum value of R2 also repeats at that same period – even though this root goes to zero through the decay portion of a cycle. Despite the above similarity, all the individual curves of X(1) through X(4) have a different shape as seen below.

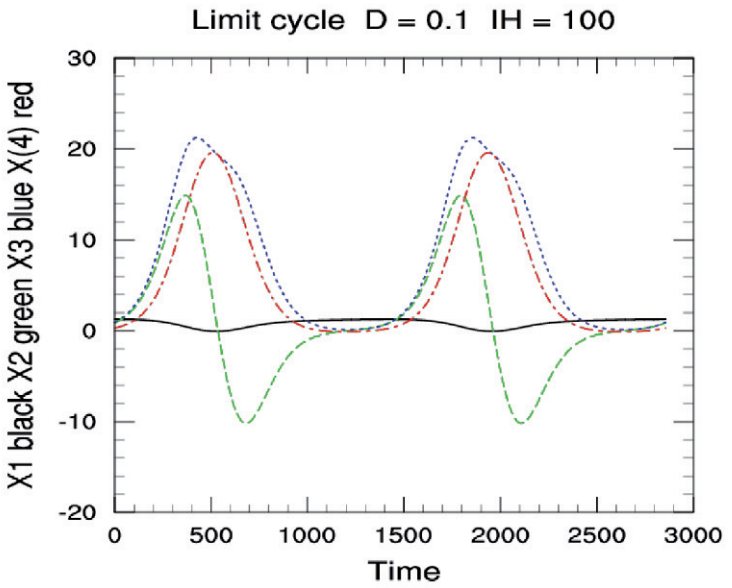

Fig. 10. Limit cycle over two consecutive periods (see text): X(1) solid black. X(2) dashed green, X(3) dotted blue, X(4) dot-dash red.

Fig. 10 indicates **two complete cycles** of the four variables. [These two cycles (each cycle is 1427 iterations) were chosen at random from the run with **D = 0.1** and **H = (1.0) H** – run out to 524288 iterations – any two cycles would show the same results seen in Fig. 10.]

The detail in Fig. 10 is discussed in the next chapter. Only note here that X(1) has a relatively small amplitude, but its amplitude is driven by the magnitude of the positive root R2 (not shown but with same period), which subsequently drives the other three variables.

It is X(3), which has the largest amplitude of the variable set, that represents the kinetic energy in the unstable wave and serves as a proxy for subsequent storm intensity.

The greater the magnitude of X(3), the stronger the **intensity** and **duration** of the subsequent precipitation event (rain, snow, or mixture) associated with the baroclinic instability.

One should be able to analyze an exact formula for that limit cycle period, but it is complicated by the changing root structure discussed above. A typical limit cycle for R1 and R2 versus X(1) was shown in the right side of Fig. 9. Thus, part of the period there is growth via the power of R2, and in most of the period there is decay via R1 and the real part of the complex roots.

From the detail in F14, It is evident that the magnitude of the roots are proportional to **(H / D).** Using this and a correction factor, the frequency (σ) of the single limit cycle is given approximately by:

σ of L_1 = (H / D) + (D - 0.102) + (0.04838 – H); with the period: P = 2 π / σ

Table 4 indicates the accuracy of this formula. The % relative error is shown as the bottom number and the top number is the period for the single-period limit cycle.

The time step is 0.01, so the period is the number of iterations divided by 100. The period in actual days is found by multiplying the period in the Table by 1.3.

The single-period limit cycles range from 24.1 days for the sluggish dynamic system (low **H** and high **D**) to 16.5 days for the fast dynamic system (high **H** and low **D**). The relative error is less than 1% for all the cases – except in the region of low **H** and high **D** where the relative error is less than 3%.

H = D =	0.8	0.85	0.90	0.95	1.0	1.05	1.10	1.15	1.20
0.120	18.54 2.84	17.82 2.08	17.17 1.45	16.58 0.96	16.04 0.55	15.54 0.21	15.09 0.01	14.56 -.21	14.27 -.31
0.118	18.33 2.34	17.62 1.64	16.99 1.15	16.40 0.67	15.87 0.34	15.38 0.01	14.93 -.11	14.51 -.25	14.11 -.40
0.116	18.14 1.97	17.43 1.29	16.81 0.88	16.23 0.47	15.69 0.09	15,21 -.09	14.76 -.26	14.35 -.32	13.96 -.39
0.114	17.93 1.52	17.24 0.97	16.62 0.57	16.05 0.24	15.52 -.55	15.04 -.23	14.60 -.31	14.19 -.36	13.81 -.35
0.112	17.73 1.16	17.04 0.63	16.43 0.30	15.86 -.01	15.35 -.17	14.87 -.33	14.44 -.33	14.03 -.36	13.65 -.34
0.110	17.52 0.77	16.85 0.38	16.23 0.08	15.68 -.17	15.17 -.31	14.71 -.32	14.27 -.38	13.86 -.40	13.49 -.30
0.108	17.32 0.48	16.65 -.09	16.03 -.13	15.50 -.29	15.00 -.35	14.53 -.42	14.11 -.32	13.70 -.34	13.34 -.15
0.106	17.10 0.11	16.45 -.14	15.86 -.29	15.31 -.44	14.81 -.49	14.36 -.40	13.93 -.37	13.54 -.08	13,02 0.12
0.104	16.90 -.12	16.25 -.34	15.66 -.48	15.12 -.55	14.63 -.52	14.18 -.42	13.77 -.24	13.38 -.08	13.02 0.12
0.102	16.69 -.36	16.05 -.51	15.47 -.56	14.94 -.55	14.46 -.44	14.01 -.33	13.66 -.14	13.21 0.02	12.86 0.31
0.100	16.48 -.55	15.84 -.69	15.28 -.60	14.75 -.58	14.27 -.46	13.83 -.27	13.43 .009	13.05 0.25	12.70 0.55

Table 4. The top number in each box is the limit cycle period (multiply by 1.3 to obtain the actual period in days); the bottom number is the error as a % of signal of the period from the formula indicated in the text.

It is extremely difficult to imagine any value of **D ≤ 0.10**, but for mathematical completeness the scatter plots for the single-period limit cycle for **D = 0.09 and 0.07 are shown in Fig. 11. When D = 0.05 and lower there are no limit cycles.**

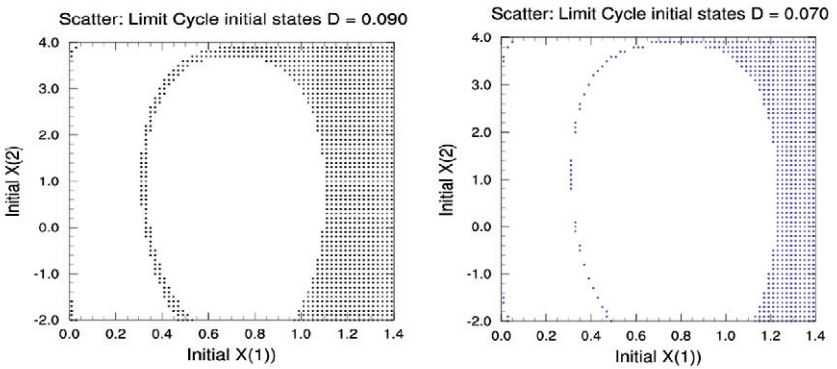

Fig. 11. Limit Cycle solutions in the X(1) – X(2) plane with X(3) = 4.0. D = 0.090 on left and D = 0.070 on the right.

5.2 A closer look at the limit cycle

It has been shown that the limit cycle is an attractor when the values of **H** decrease from some very large value down to values approaching the current atmospheric differential heating. Also the case of decreasing values of **D** also led to a limit cycle attractor. Further in F14, one was able to adjust values of the variables themselves to achieve a temporary limit cycle. When the atmosphere is in a mode of ice age physics (discussed in Chapter 8) the differential heating between the equator and the poles may increase. In an actual ice age, the large extent of ice coverage may induce less friction. In either case the probability of an occurrence of a temporary limit cycles may occur. The cycle itself is as close to an analytical solution for the nonlinear process of baroclinic instability as one might get. Thus, it is worth looking at in some more detail.

Fig. 10 showed the values of the four variables over two consecutive periods. Each variable X(1) through X(4) has a distinct maximum and minimum value within a cycle, and these maximum and minimum values repeat for each variable with every period – in the same relative position. The phase relationship, with X(1) leading the other variables is the exact same for each cycle. The right side of Fig. 9 indicated the R1 and R2 roots on the same plot versus X(1). It is clear that the R2 root is not always present.

The R2 root is important because if the critical value for this root is not exceeded, the solution for the system is vacillation with the ultimate attractor is the fixed point solutions for the four variables. In a limit cycle the X(1) maximum follows the R2 root maximum by 69 iterations; the X(2) maximum follows the X(1) maximum by 366 iterations; the X(3) maximum follows the X(1) maximum by 426 iterations; and the X(4) maximum follows the X(1) maximum by 508 iterations.

The basic shape of X(1) versus X(2) has an unusual shape (a unique curve) in three different attractors in the lower right corner. Notice the left side of Fig. 6 for vacillation, the right side of Fig. 6 for chaos, and the left side of Fig. 9 for the Limit cycle (the scale on these Figs. are all different, and the limit cycle is larger than chaos in this particular run because of the small value of friction).

The strange shape in each of these Figs. comes primarily from X(2) which approaches zero from its negative value in a very slow manner and then remains near zero – far from the action of a single sine or cosine wave. All four variables are perhaps decomposable into a multitude of wave forms. However, X(3) is quite unique – it has a strange indentation in Fig. 10 just past its max value where it has the same value as X(4) when X(2) = 0.0 (this is discussed in the next chapter).

The second possible solution to these model equations, discussed in more detail in Chapter 6.6, is the unstable zonal solution which would have X(2), X(3), and X(4) all = 0.0. It is a strong attractor as seen in the chaos trajectory shown in Fig. 6. These three variables remain near zero as X(1) is growing in value. The critical area of unique curvature is best seen in the chaos image of Fig. 6 where there is extreme convergence of the trajectories – these are chaotic trajectories which implies that they are infinitely close but never cross each other.

5.3 The fractal dimension of the attractor

In addition to the five attractors discussed above (two are unstable), there is a sixth attractor in this model. There is an attractor within an attractor (this is discussed in Appendix 4). There is an innocuous attractor involving X(4) within the strange attractor of the system. It is shown in Appendix 4 that any initial state of the system will approach the hypersurface:

$X(3)^2 = X(2)^2 + X(4)^2$

If the phase point were initially on the surface, it will stay on the surface. This is an equation for a cone, which is another attractor. The above relation was evaluated at every iteration in several runs and compared with the predicted value of X(4) from the eq. set (4). In a limit cycle run it was still accurate after 100,000 iterations to 10 decimal places. In a similar 100,000 integration time for a chaos run, the value of X(4) was still accurate to 9 decimal places. Fig. 12 shows the cone attractor in a chaos run – it is an attractor within a strange attractor. It remains a cone throughout a limit cycle solution or a vacillation solution as well. The variable X(4) does not affect the stability of the system.

The three real roots from F14 (e.g., when root R2 is a maximum) provide the following ordering of the roots: (0.4423, 0.03, - 0.899). Using the Kaplan-Yorke conjecture for the upper bound of the fractal dimension of the attractor which is based upon arranging the Lyaponov exponents in order from largest to smallest $\lambda_1 \geq \lambda_2 \geq \lambda_3 \ldots \lambda_n$. Then when J denotes the number of positive roots:

$\sum^{J}_{i=1} \lambda_i > 0$ and $\sum^{J+1} \lambda_i < 0$ are valid, then the dimension of the attractor is determined as follows:

$D = J + \sum^{J}_{i=1} \lambda_{i\,i} / | \lambda_{J+1} |$

Thus D = 2 + (.4423 + .03) / 0.899 = 2.53.

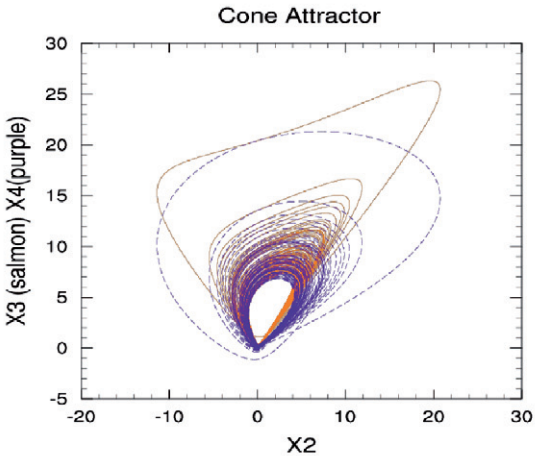

Fig. 12 Cone attractor in chaos: X(2) vs X(3) (solid salmon line) and X(4) (dashed purple line).

5.4 The hybrid chaotic solution that destroys itself

There is a seventh (hybrid) attractor in this model. Another solution has been found in the 40,000 **deterministic** runs which were tested prior to performing the SDE/MC approach to this model. When the chaos becomes too intense, a sequence of mathematical events sends the solution back to the fixed point attractors of the model – just as if the solution had been one of vacillation to begin with.

Fig. 13 (which only indicates results from 200,000 to 300,000 iterations) clearly exhibits the **original chaos, the maverick long period, large magnitude X(3),** then the rapid transition to the vacillation solution with X(3) eventually reaching its fixed point value of 2.748**. This only occurred three times in the 40,000 sample size so it is a rare event**. Each time the three solutions return to the same fixed point values – as expected for all vacillation solutions. Why this occurs will entail recalling a few details from F14.

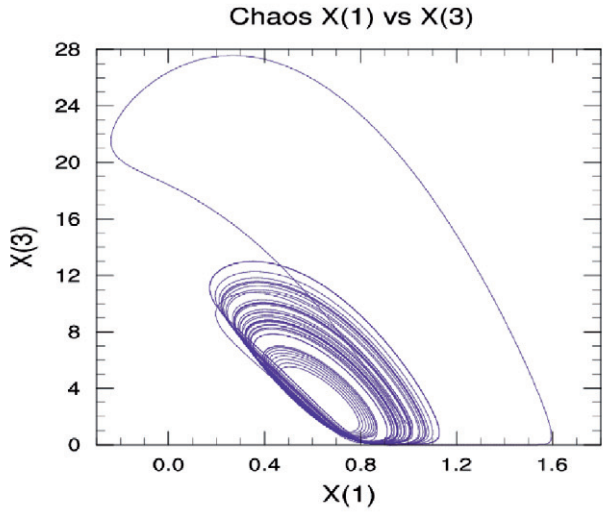

FIG. 13 Original chaotic attractor of 200,000 + iterations produces a renegade X(3) and the stability of the system responds by generating a vacillation solution (see text).

One of the attractors of this model is the zonal solution of X(1) = H/LD and X(2) = X(3) = X(4) = 0.0. This solution was discussed in Chapter 5. This solution is strongly attracting as seen in the chaos runs shown in Fig. 6. However, the zonal solution is unstable and X(1) never reaches its theoretical max value of H/LD = (.042253)/ (.065) (.202) = 3.218. From the prognostic equation for X(1) it is evident that the change is smaller as X(1) gets larger. The growth of X(1) is curtailed near to X(1) = 1.6 in Fig. 13. The large value of X(1) at its maximum has increased the magnitude of the positive root R2 (see example of the right side of Fig. 8.) and hence the extreme value of X(3) shown in Fig. 13.

The three real roots for the model only occur when $Q^3 - R^2 > 0$. The values of Q and R as a function of the variables (see **F14** for details) are provided below:

$Q = 0.1456 - (0.0127)\, X(3) + X(1)^2$

$R = -0.02185 + (0.0012)\, X(3) + (0.01904)\, X(1)\, X(2) + (0.06295)\, X(1)^2$

The left side of Fig. 14 shows the growth of Q with the increase of X(1), but as X(1) decreases to near zero (even becoming slightly negative), **and** the effect of the large X(3), make Q become **quite** negative. The right side of Fig. 14 indicates X(1) versus R and now both Q and R remain low with $Q^3 - R^2 < 0$ and the real roots give way to the complex roots.

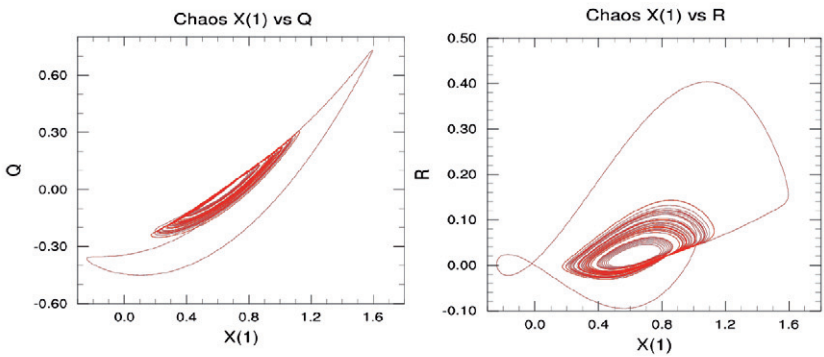

Fig. 14 X(1) vs Q on the left and X(1) vs R on the right (see text for details)

Fig. 15 indicates Q versus R. In the lower left corner of the figure one observes both Q and R as negative - after this very stable event, the roots remain complex and the vacillation cycle takes over. The author refers to this as a hybrid attractor as it maintains itself in both states for two equally long periods.

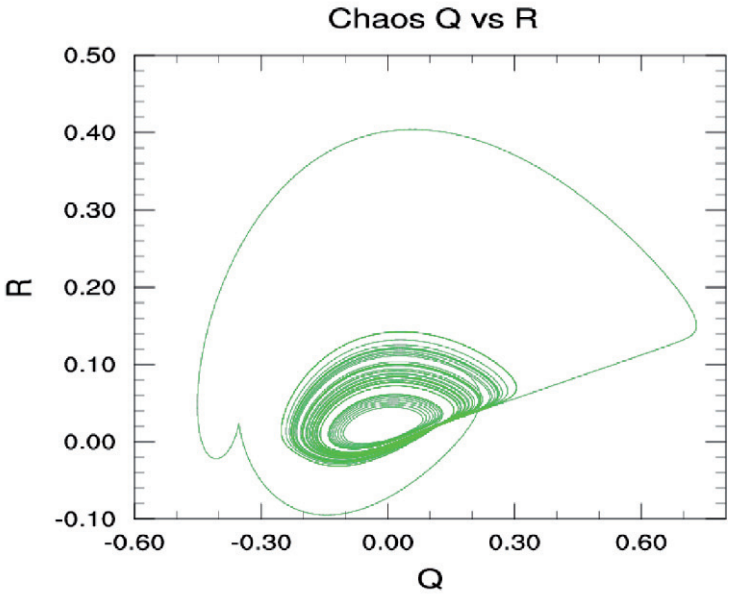

Fig. 15 Q versus R in the renegade hybrid attractor that converts from chaos to vacillation.

There is no indication of numerical instability in these results – all the calculations are stable and the cone equation is satisfied still to nine decimal places at iteration 200,000 and at 300,000.

There also is nothing special about the random normal deviates. The three different deviates that produced three different hybrid solutions like that shown in Fig.13 are shown in bold font below surrounded by the previous and subsequent deviates.

There is no special attention due to either the sign or the magnitude (note that not all the digits are shown in order to save space.)

# 11513 = -.4428681 x 10^{-3}	# 25851 = .4818583 x 10^{-3}	# 34764 = -.1775111 x 10^{-3}
# 11514 = .3345724 x 10^{-3}	**# 25852 = -.1337233 x 10^{-2}**	**# 34765 = -.2177961 x 10^{-2}**
# 11515 = .1003886 x 10^{-2}	# 25853 = .1002926 x 10^{-2}	# 34766 = .1701284 x 10^{-3}

The probability of occurrence of this phenomena appears to be less than 1 in 10,000 from the deterministic input to this particular 40,000 sample size MC run.

It is also consistent with the fact that the **trace** of the roots of this system (the sum of the three real roots or the sum of R1 and the real portion of the two complex conjugate roots) is always **constant** and always **negative.** See F14 for more details. **Thus, there can never be run-away baroclinic instability.**

Chapter 6

The SDE/MC approach on the explosive baroclinic attractor

The values for the chaotic solution used for the initial conditions for Table 3 will be used as the basis for the SDE/MC approach to the chaotic solution for the equation set **(4).** These values were (0.4, 0.0, 0.25, 0.25) for the four variables and **D = .202** and **H = (1.0) H** -- the conditions of today's atmosphere.

A few of the stochastic dynamic equations for equation set **(4)** are listed below (the reader should be able to complete the rest with instructions given above in Chapter 2):

$\partial\, \mu(1)/\, \partial t = -LR\, \mu(2) - LD\, \mu(1) + H$

$\partial\, \mu(2)/\, \partial t = \mu(1)\, \mu(3) + \sigma(1,3) - D\, \mu(2) - R\, \mu(4)$

$\partial\, \mu\, (3)/\, \partial t = \mu(1)\, \mu(2) + \sigma(1,2) - D\, \mu(3)$

$\partial\, \mu(4)/\, \partial t = R\, \mu(2) - D\, \mu(4)$

$\partial\, \sigma(1,1)/\, \partial t = -\, 2\, [\, LR\, \sigma(1,2) - LD\, \sigma(1,1)]$

$\partial\, \sigma(1,2)/\, \partial t = -LR\, \sigma(2,2) - LD\, \sigma(1,2) + \mu(1)\, \sigma(1,3) + \mu(3)\, \sigma(1,1) + T(1,1,3) - D\, \sigma(1,2) - R\, \sigma(1,4)$

$\partial\, \sigma(1,3)/\, \partial t = -LR\, \sigma(2,3) - LD\, \sigma(1,3) + \mu(1)\, \sigma(1,2) + \mu(2)\, \sigma(1,3) + T(1,2,3) - D\, \sigma(3,3)$

$\partial\, \sigma(3,3)/\, \partial t = 2\, [\, \mu(1)\, \sigma(2,3) + \mu(2)\, \sigma(1,3) + T(1,2,3) - D\, \sigma(3,3)]$

$\partial\, T(3,3,3)/\, \partial t = 3\, [\, \mu(1)\, T(2,3,3) + \mu(2)\, T(1,3,3) - \sigma(1,2)\, \sigma(3,3) + \lambda(1,2,3,3) - D\, T(3,3,3)]$

$\partial\, \lambda(3,3,3,3)/\, \partial t = 4\, [\, \mu(1)\, \lambda(2,3,3,3) + \mu(2)\, \lambda(1,3,3,3) - \sigma(1,2)\, T(3,3,3) + f(1,2,3,3,3) - D\, \lambda(3,3,3,3)]$

The MC sample size will be large (40,000) with Gaussian deviates added to the initial state of X(1). The chaotic solution with this initial state run out to 2^{19} = 524,288 iterations is shown in Figs. 16 with X(1) vs X(2) and X(1) vs X(3) indicated on the left and right side of the figure, respectively.

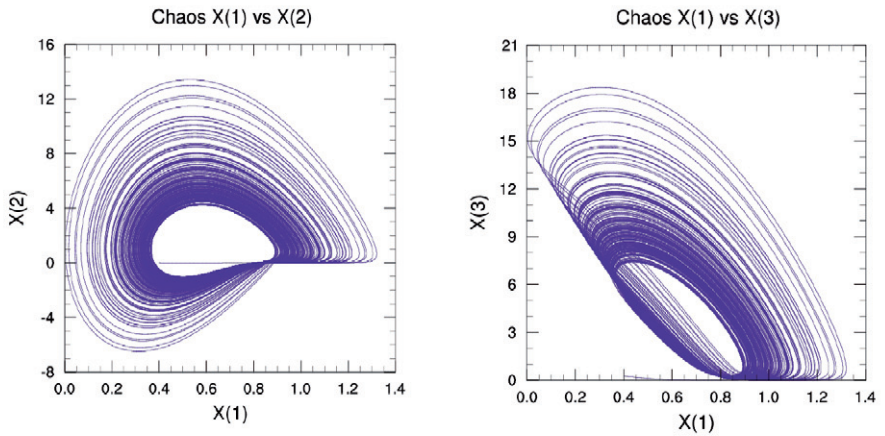

Fig. 16 Monte Carlo basis run: chaos with initial conditions (0.4, 0.0, 0.25, 0.25)

Care must be taken in the Monte Carlo initial states chosen as explained here. In the Lorenz attractor the cycle was only about 70 iterations and the averaging time was over 4000 iterations of a MC sample size of 40,000. This provided an averaging time of order 60 times the typical period of the chaotic oscillation. The averaging time in the explosive baroclinic attractor must be considerably longer as the typical period of a chaos cycle has an average minimum of 1365 iterations and an average maximum of 3330 cycles – some cycles can be considerably longer.

Thus, achieving a comparable averaging time for the EBI attractor would entail some 60 x 3330 = 199,800 iterations. Being conservative, the integration time for all the MC runs in this Section was 2^{19} or 524,288 iterations.

Now with such a long integration time, there is concern about round off error with a finite computer word size. It was stated above that the value of X(4) in the cone equation was accurate to 9 decimal places in a long term chaos calculation. All calculations in this study are performed in double precision, so this is very good, but perhaps still not sufficient for this model calculation because of another factor.

There is another attractor and solution in this model: $X(1) = -(R^2 + D^2)$. As discussed earlier, this solution is shown to be unstable in Appendix 3. If X(1) became **sufficiently negative** it would lead to X(3) becoming negative which is physically unrealistic (see F14 on how the model avoids this). Nevertheless, it is an attractor, and one observes X(1) approaching zero and even becoming slightly negative in some runs. When this occurs, X(3) could possible become negative through round off error.

The variable X(3) represents kinetic energy which must always be positive. Observing the value of X(3) in Fig. 16 it is seen that it comes very close to zero on part of its cycle. A test was made to check on the X(3) possibly crossing the zero value due to round off error. The test was worth doing as on a very few occasions, the value would just slightly become negative. When this occurred the result could be benign, but usually lead to an eventual blowup of the solution. Reducing the time step by a factor of two would not eliminate all such initial states. The decision was made to just test for and eliminate those random deviates that gave the problem.

A special pre-run was performed on all random initial states – checking on **every iteration** for a negative X(3) in each of the 40,000 deterministic runs. When this occurred that random initial state was so marked and removed from the subsequent MC run. As the length of the integration was extended in time, the number of such potentially bad initial states increased—as one would expect.

The results in this study found 341 potentially bad initial states out of 40,000 initial random states in an integration to 524,288 iterations. None of those potentially bad initial states were used in the MC integration, so that the final number that were used was 39,659. The subsequent variability of the results in these 39,659 initial states is due to chaos and not round-off error.

The check on X(4), as described above, was also found to be accurate to 9 decimal places for each of these initial states. Each of these runs produced the typical chaos first return map as seen in Lorenz (1963) , seen in the Rössler attractor in the left side of Fig 4, and shown for this attractor in Fig. 17.

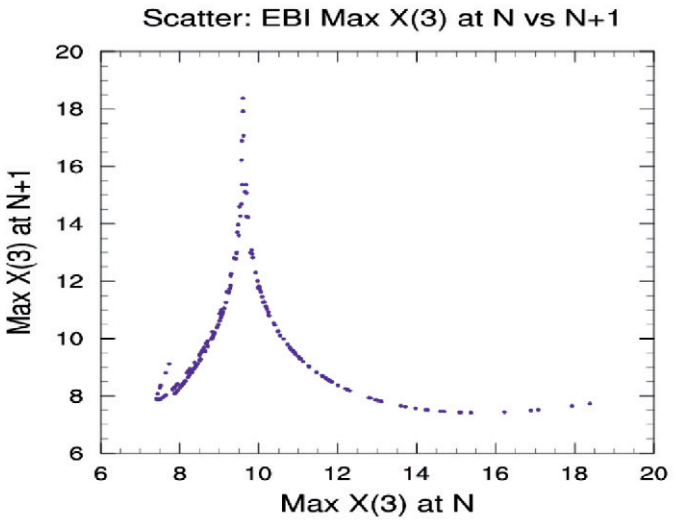

Fig. 17 The typical chaos first return map for initial states used in the basis run